



Sodium-Dictated Free-Standing Lignin-Carbon Electrode towards Ultrahigh Capacitance

Manish Neupane^{+[a]} Qiangu Yan^{+[b]} Rui He,^[c] Rihab Masmoudi,^[d] Yifeng Liu,^[e] Zoe Benedict,^[a] Jinwu Wang,^[b] Carl Tripp,^[d] Pei Dong,^[c] Zhiyong Cai,*^[b] and Yingchao Yang,*^[a]

Lignin is a waste product in the paper industry and lignocellulosic biorefineries, in addition to being the second most abundant renewable biopolymer on Earth. Valorization of useless lignin into high value-added advanced materials not only helps address the environmentally detrimental biowaste but also satisfies the societal need for energy. While lignin has been converted into porous carbon, made into slurry, and pasted onto metal forms as an electrode for lithium-ion batteries and supercapacitors, there remains issues with how to scale up the process while achieving great area and mass capacitances in the fabricated lignin-carbon electrodes. In this

work, a thick freestanding electrode coupled by lignin carbon and sodium without any binder and additives was fabricated demonstrating a specific area capacitance of 19.7 F cm^{-2} at a current density of 1 mA cm^{-2} , which is the highest among to date reported freestanding lignin carbon electrodes with similar thickness. This excellent electrochemical performance originates from high electro-positivity and oxygen content promoted by the sodium. This work brings a new strategy towards lignin utilization and energy storage through coupling lignin carbon and alkali metals.

Introduction

Lignin is the second most abundant biopolymer and the most abundant aromatic-containing polymer in nature. Typically, lignin accounts for 15%–30% of plants and serves as an adhesive by forming a lignin-carbohydrate complex to bind cellulose and hemicellulose together.^[1,2] Lignin is a waste product in the production of paper or chemicals (e.g., ethanol) from biomass. If not removed, the lignin could cause the paper-derived wood pulp to weaken and discolor rapidly.^[3] Valorization of useless lignin to high value-added materials for advanced applications would help address the environmentally

detrimental biowaste and satisfy the societal need. To date, lignin has been used as a functional component in polymer synthesis. For example, polyhydroxyalkanoate (PHA)/lignin shows better microbial resistance than PHA alone due to the formation of strong hydrogen bonds.^[4] Lignin blended poly-lactic acid (PLA) exhibits a great non-flammable capability.^[5] Furthermore, monomers in lignin have been used to synthesize polymers, such as polyester and polyurethanes.^[6–8] However, owing to the chemically recalcitrant nature, it is very challenging and costly to convert lignin into value added biopolymers.

Recently, the focus on using lignin and its derivatives has been shifted to fabricating electrodes for energy storage devices, including lithium-ion batteries and supercapacitors. Regarding batteries, lignin has been used by either combining it with additives and binders as electrodes for lead-acid batteries or by fabricating it into three-dimensional (3D) hierarchical porous carbon as electrodes for lithium-ion batteries.^[9–12] Without a doubt, the lignin-based electrode is cheaper and greener alternative to existing electrodes.

In addition to batteries, porous carbon made from lignin has been investigated as a potential electrode for supercapacitors. For example, lignin was converted to porous carbon electrode activated by sodium hydroxide for supercapacitors, giving a galvanometric capacitance of 267.8 F g^{-1} at current density of 50 mA g^{-1} .^[13] The common approach in using lignin carbon to fabricate electrode for supercapacitors is slurry-paste strategy. After the lignin carbon particles are collected, the conventional binder material, such as polyvinylidene fluoride (PVDF) or polytetrafluoroethylene (PTFE), along with a solvent like N-methyl-2-pyrrolidone (NMP), are used to bind the carbon particles together, forming a freestanding electrode after drying the paste onto a nickel (Ni) or stainless-steel mesh. The lignin porous carbon coated on the stainless steel has the capacitance of 165 F g^{-1} at a current density of 0.05 A g^{-1} .^[14] Similarly, lignin

[a] M. Neupane,* Z. Benedict, Prof. Y. Yang
Department of Mechanical Engineering
University of Maine
75 Long Road, Orono, ME 04469 (USA)
E-mail: yingchao.yang@maine.edu

[b] Dr. Q. Yan,* Dr. J. Wang, Dr. Z. Cai
Forest Product Laboratory, U.S. Department of Agriculture
1 Gifford Pinchot Drive, Madison, WI 53726 (USA)
E-mail: zhiyong.cai@usda.gov

[c] Dr. R. He, Prof. P. Dong
Department of Mechanical Engineering
George Mason University
4400 University Drive, Fairfax, VA 22030 (USA)

[d] R. Masmoudi, Prof. C. Tripp
Department of Chemistry
University of Maine
154 Aubert Hall, Orono, ME 04469 (USA)

[e] Y. Liu
Department of Materials Science and NanoEngineering
Rice University
6100 Main Street, Houston, TX 77005 (USA)

[+] These authors contributed equally to this work.

Supporting information for this article is available on the WWW under <https://doi.org/10.1002/batt.202300193>

derived pyrrole modified electrode on Ni mesh shows the capacitance of 248 F g^{-1} at current density of 0.1 A g^{-1} .^[15] Although the lignin carbon shows a good capacitance values, a few well-known disadvantages includes (1) the amount of lignin carbon in an individual electrode is marginal; (2) the binders and solvents used to prepare electrode are expensive and not environmentally friendly; and (3) additives such as carbon black or acetylene black are needed to compensate for the lack of conductivity of the binders. To take advantage of abundant biowaste lignin, it will be beneficial to directly fabricate free-standing electrode with lignin but without any binder and additives for supercapacitors. For example, a free-standing lignin carbon electrode was fabricated with Pluronic P123 polymer as a template and silica as a pore generator, which exhibited an area capacitance of 6.20 F cm^{-2} at a current density of 1.4 mA cm^{-2} .^[16] Furthermore, lignin was hydrothermally converted into an electrode in the presence of Ni-foam to get a thick electrode, where area capacitance was 5.88 F cm^{-2} at 1 mA cm^{-2} .^[17] Currently, it is still challenging to obtain a thick electrode with high mass loading, simultaneously, maintaining an outstanding area and mass capacitances. Learning from the fabrication of electrodes from other biomasses, electrode capacitance can be benefited by improved porosity, wettability, and conductivity via coupling metal oxides with porous carbon, doping carbon with nitrogen heteroatoms, and generating functional group.^[18–20]

Sodium (Na) has been explored as a potential alternative to lithium in energy storage, due to its similar electrochemical properties, low cost, and abundance in the earth's crust.^[21–23] Compared to other alkali metals, sodium ions have the smallest size difference with respect to lithium ions, which allows them to easily intercalate into similar electrode materials and participate in reversible electrochemical reactions. However, the use of sodium in energy storage also presents the challenge on electrode stability degradation.^[24] Therefore, a new material design is needed to optimize the use of sodium in energy storage in order to realize its full potential as a viable alternative to lithium. The combination of sodium and lignin carbon can provide good stability and resistance to degradation over multiple charge-discharge cycles, which is important for practical energy storage applications. In addition, the alkali metals could further increase OH^- accumulation on surface improving the capacitance substantially.^[25]

In this study, a thick freestanding electrode was fabricated with sodium incorporated into lignin carbon yet without any binder and additives. The electrode demonstrates excellent electrochemical performance with the specific capacitance reaching 19.7 F cm^{-2} at a current density of 1 mA cm^{-2} , which is higher than that of reported freestanding lignin carbon electrode with similar thickness. The excellent electrochemical

performance originates from the large amount sodium in lignin carbon offering higher electro-positivity and oxygen contents in the electrode. After 5000 charge-discharge cycles, the capacitance of lignin carbon exhibits 99.5% retention rate, which well addresses the challenge of electrode stability degradation faced previously.

Results and Discussion

Porous lignin carbon was fabricated via controlled carbonization parameters with various concentrations of sodium, including approximately 1 wt. % (LCF #1), 8 wt. % (LCF #2), 16 wt. % (LCF #3), and 28 wt. % (LCF #4), resulting in carbon materials with distinct morphologies and electrochemical properties. The morphology and composition for LCF #2 and LCF #4 can be found in the Supporting Information Sections 1 and 2. Figure 1 compares morphology and element distribution of the most representative specimens LCF #1 and LCF #3. Shown in Figure 1(a), LCF #1 has macropores with size between $50 \mu\text{m}$ and $150 \mu\text{m}$. The high magnification scanning electron microscopy (SEM) image in Figure 1(b) shows a smooth surface without significant volume defects. In contrast, LCF #3 has a particle-like microstructure with a particle sizes distribution from tens of nanometers to tens of micrometers (Figure 1g and h). The difference in morphology between LCF #1 and #3 is due to the variation of sodium amount. Sodium ions can act as a catalyst for the carbonization process by promoting breakdown of lignin into carbon.^[26] The more sodium participates in the reaction, the smaller carbon particles with nonuniform sizes will be obtained.^[27] Furthermore, sodium may form sodium carbonate at low temperatures, which may have a significant impact on the structure of carbon materials produced from lignin precursors. When temperature is elevated during the carbonization process, the carbonates will decompose into Na_2O and CO_2 , where CO_2 reacts with carbon to form micropores and Na_2O is reduced by carbon, forming vapors of sodium and further promoting micropores formation in carbon.^[23,28–30] Both reaction mechanisms will facilitate the generation of small particles observed in Figure 1(h), thus, resulting in a porous carbon. This is evidenced with the XPS analysis on LCF #1 and LCF #3 (before acid treatment) listed in Supporting Information Section 3. A prominent carbonate peak was observed in LCF #3 whereas no such peak was evident in LCF #1. The existence and structure of sodium compounds will be carefully discussed through the X-ray diffraction (XRD) and X-ray photoelectron spectroscopy (XPS) analyses in the later Section.

The composition and distribution of both LCF #1 and LCF #3 were characterized by EDS mapping, demonstrated in Figure 1(c–f) and Figure 1(i–l), respectively. Table 1 summarizes

Table 1. Atomic and weight percentages of each element in the lignin carbon.

C [at. %]	O [at. %]	Na [at. %]	S [at. %]	C [at. %]	O [at. %]	Na [at. %]	S [at. %]
LCF #1	94.94	4.21	0.45	0.25	92.69	5.47	0.84
LCF #3	60.53	28.37	10.34	0.76	50.38	31.45	16.47

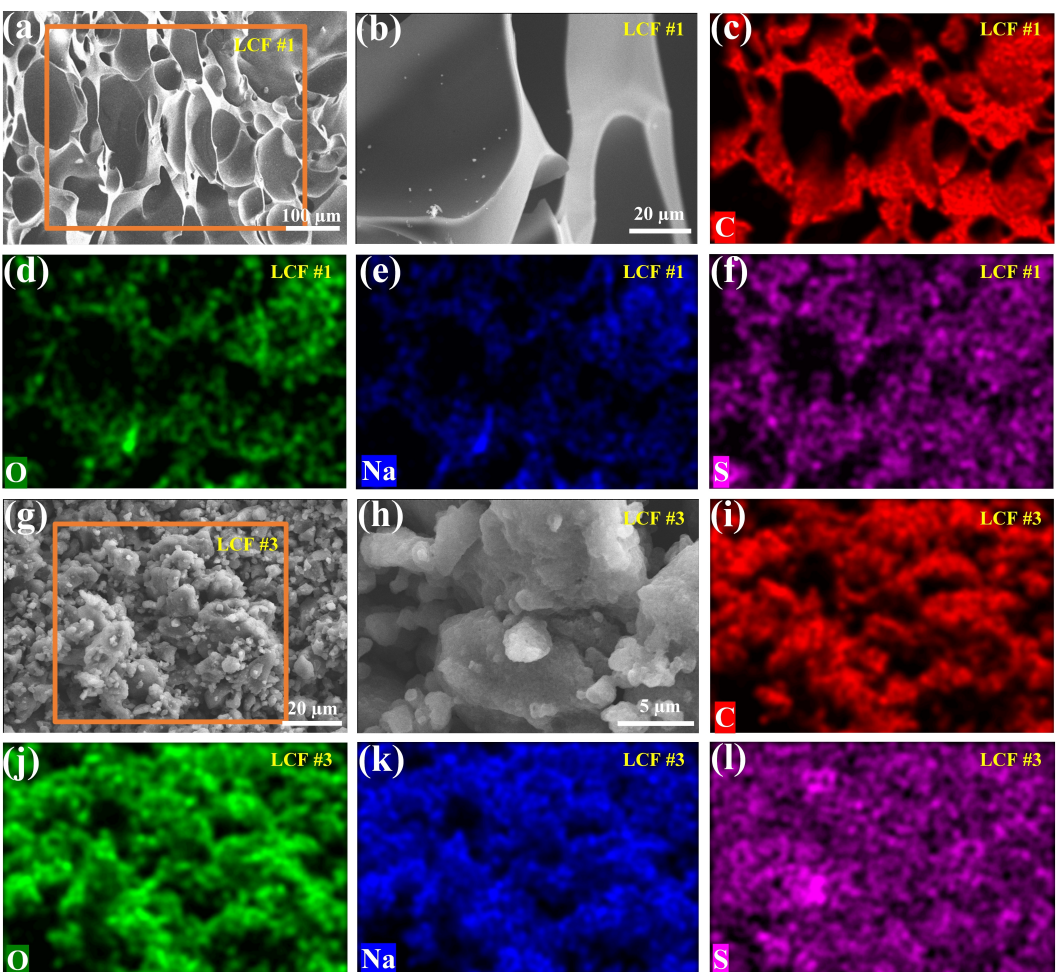


Figure 1. Morphology and composition of lignin carbon incorporated with sodium. a, b) SEM images of LCF #1. c-f) EDS mapping of LCF #1. g, h) SEM images of LCF #3. i-l) EDS mapping of LCF #3.

the elements and their atomic and weight percentages in the specimens. LCF #1 and LCF #3 have elements of carbon, oxygen, sodium, and trace elements, such as sulfur and aluminum from lignin. All elements are uniformly distributed throughout the specimens. The detected sodium atomic percentages in LCF #1 and LCF #3 are 0.45% and 10.34% respectively. Meanwhile, the oxygen atomic percentages are 4.21% and 28.37% respectively. As the oxygen content increases substantially when the percentage of sodium is increased, it suggests that most of sodium is not in a free form, but in compounds, such as sodium oxide, sodium hydroxide, and sodium carbonate. In turn, this allows more oxygen to be trapped in the lignin carbon. The rich oxygen in carbon materials can improve their electrochemical properties by introducing additional surface functionalities and increasing the number of active sites for charge storage.

To fully understand the structure and surface of LCF #1 and LCF #3, surface structure was determined by XRD, Brunauer–Emmett–Teller (BET) analysis, and XPS. The XRD patterns for LCF #1 and LCF #3 are shown in Figure 2(a). The XRD peaks obtained around 25°, 43° and 78° can be respectively assigned to (002), (101) and (110) carbon planes.^[31] Unlike LCF #1, LCF #3

has multiple sharp peaks from 30° to 40°. The sharp peaks at 32°, 35° and 40° can be respectively assigned to (202), (120) and (441) crystallographic planes of hydrated sodium carbonates.^[32] Figure 2(b and c) exhibits N₂ adsorption/desorption isotherms and pore size distribution respectively. The pore size distribution in LCF #1 is majorly confined within the range of 2.7–4 nm, suggesting the limited presence of micropores, whereas LCF #3 consists of a more broad pore distribution from 2.5 to 10 nm. This hierarchical distribution of micropores and mesopores throughout smaller particles shown in Figure 1(h) in LCF #3 may promote energy storage in the fabricated supercapacitors. Mesopores can provide access to the inner surface and facilitate diffusion of ions into micro pores, enabling faster charge-discharge rates,^[33] while micropores offer a high surface area for charge storage. The specific surface area (SSA) and pore volume of these samples were calculated. The SSA for LCF #1 and LCF #3 are 12.99 m² g⁻¹ and 64.19 m² g⁻¹, respectively, suggesting that the LCF #3 fabricated electrode may have higher capacitance as more surface area is formed in the specimen.

The surface elemental groups and level of defects on both LCF #1 and LCF #3 were first investigated by Fourier transform

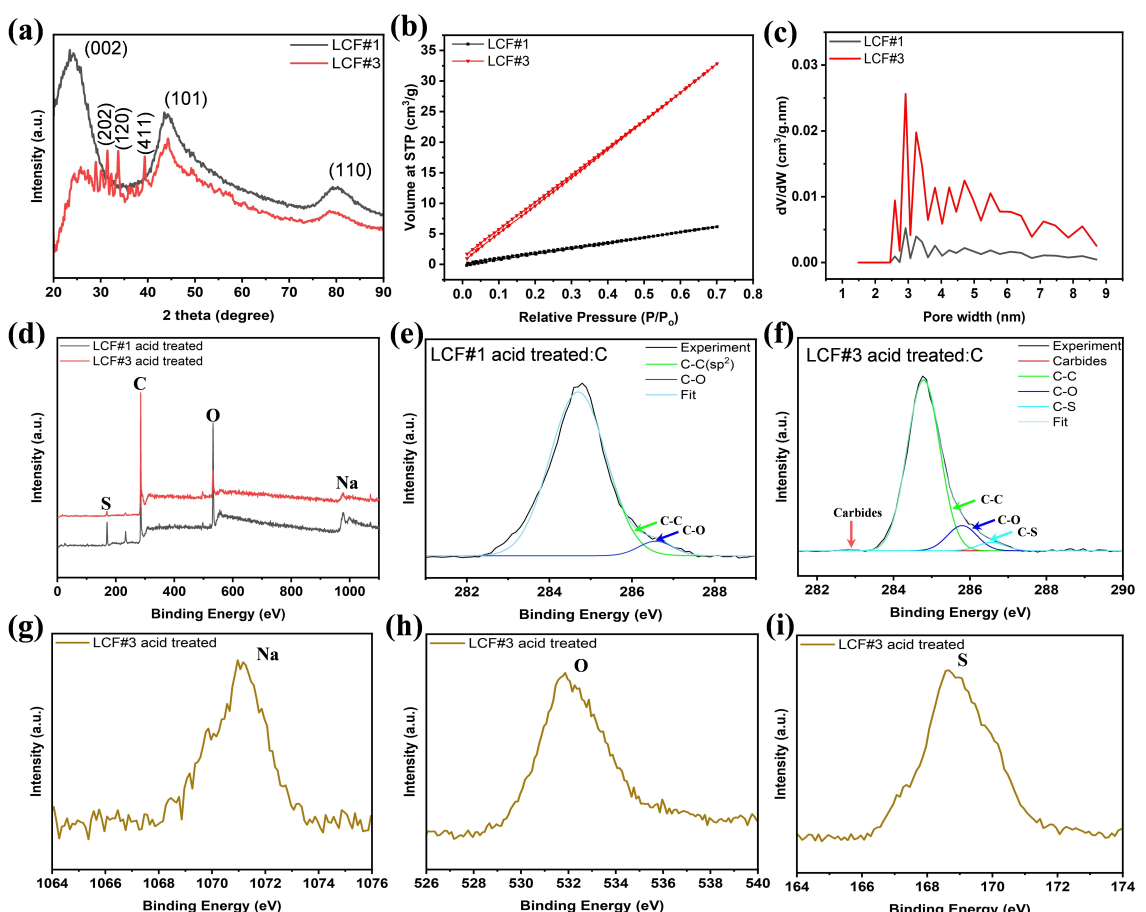


Figure 2. Structure and surface characterization of LCF #1 and LCF #3. a) XRD spectra, b) N_2 adsorption/desorption isotherms. c) Density functional theory (DFT) pore size distributions. d) Full scale XPS survey. e, f) Deconvolution of the C 1s core level spectra. XPS spectra of g) Na, h) O, and i) S.

infrared spectroscopy (FTIR). The results and figures can be found in the Supporting Information Sections 4 and 5. Then the functional groups were carefully evaluated and quantified using XPS (Figure 2d and e). A full scale XPS survey of samples after acid treatment reveals the presence of C, Na, O and S. Figure 2(e) and f) demonstrate the deconvoluted C1s spectra for LCF #1 and LCF #3, respectively. As shown in Figure 2(e), the C1s spectrum for LCF #1 can be deconvoluted into two Gaussian curves with peaks at 284.8 eV and 286.5 eV corresponding to C–C (sp^2) and C–O, respectively. The C–O peak suggests the hydroxylation of the sample due to acid treatment, making it hydrophilic. Similar C–O peaks were previously observed after treating balsa carbon with acid.^[33] In addition to C–C (sp^2) and C–O peaks, LCF #3 exhibits two additional peaks at 283.0 eV and 286.7 eV, which can be ascribed to the binding energy of carbides and C–S respectively. Table 2 shows bonds deconvol-

uted from C 1s and their percentage compositions of LCF #1 and LCF #3. The oxygen-containing functional groups are approximately 12% in LCF #3, which is almost doubled compared to that in LCF #1. The oxygen-containing functional groups will necessarily improve the interaction with the electrolyte and help to improve the transport of ions. The presence of approximately 4% of carbon-sulfur bonds can provide additional active sites for electrochemical reactions and can improve the overall electrical conductivity of the carbon material.^[34] Additionally, sulfur can act as a redox-active element, enabling reversible electrochemical reactions to take place during the charge-discharge processes. The spectra for sodium, oxygen and sulfur are shown in Figure 2(g–i). Lastly, water contact angle was measured for both LCF #1 and LCF #3. Due to porous structure, water droplets can be rapidly absorbed by LCF #1 and LCF #3 within 0.2 seconds. Details of water absorption scenarios can be found in the Supporting Information Section 6.

The electrochemical performance of the fabricated electrodes was measured with a three-electrode system, of which a platinum sheet was used as a counter electrode, a commercial Ag/AgCl electrode was used as a reference electrode, and 6 M KOH solution was used as the electrolyte. The potential window was set from –0.8 to 0.0 V. Figure 3 shows the electrochemical performances of LCF #1 and LCF #3 after acid treatment. The CV

Table 2. Bonds deconvoluted from C 1s and their fractions of LCF #1 and LCF #3.

Bonds	C–C sp^2	C–O	C–S	Carbide
Binding energy [eV]	284.8	286.5	286.7	283
LCF #1	94.88%	5.11%	0	0
LCF #3	84.98%	11.30%	3.48%	0.23%

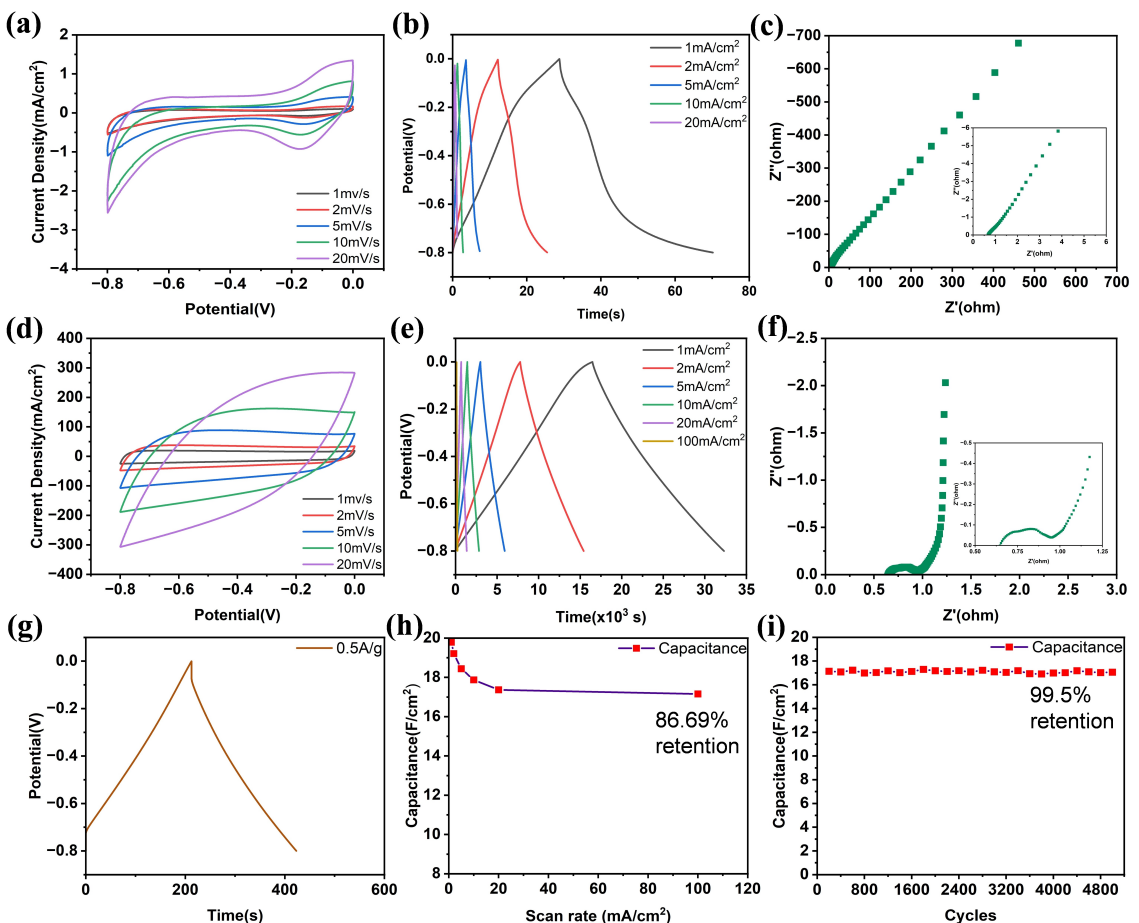


Figure 3. Electrochemical performance of LCF #1 and LCF #3. a) CV of LCF #1 at scan rates of 1–20 mV s⁻¹. b) Constant-current charge/discharge curves of LCF #1 at current densities 1–20 mA cm⁻². c) Nyquist plot for LCF #1 with inset of high frequency region. d) CV of LCF #3 at scan rates of 1–20 mV s⁻¹. e) Constant-current charge/discharge curves of LCF #3 at current densities of 1–20 mA cm⁻². f) Nyquist plot for LCF #3 with inset of high frequency region. g) GCD of LCF #3 at 0.5 A g⁻¹. h) Capacitance of LCF #3 at different current densities. i) Cyclic performance of LCF #3 at 100 mA cm⁻² for 5,000 cycles.

curves in Figure 3(a) are from LCF #1 at scan rates of 1–20 mV s⁻¹. Generally, carbon materials have near perfect rectangular CV curves, resulting from the electric double-layer capacitor (EDLC) charging and discharging mechanism. Additionally, the area enclosed between the curves indicates capacitive performance. For LCF #1, the area between the charging and discharging curves is very low, indicating poor capacitance. Furthermore, the curve is not perfectly rectangular. Instead, it contains two bumps, due to the presence of residual AgCl in the reference electrode,^[35] where the contribution to capacitance is negligible. Figure 3(b) demonstrates galvanometric charge discharge (GCD) curves for LCF #1 at different current densities. The curves exhibit in a distorted triangular shape, which could result from (I) electrode polarization and/or (II) irreversible reactions. For the electrode polarization, if there is accumulation of charge at the electrode surface due to a slow rate of charge transfer or lack of available surface area for the charge to distribute, it will lead to a non-linear charge-discharge curve, with the voltage dropping off more quickly than expected. The low surface area is confirmed by the BET analysis, where the SSA for LCF #1 is only 12.99 m² g⁻¹, which is very low compared to 64.19 m² g⁻¹ from LCF #3. When the electro-

chemical reactions taking place during charging and discharging are not completely reversible, it will bring a loss of capacity and distortion of the charge-discharge curve. The calculated value capacitance of LCF #1 from GCD is 0.052 F cm⁻² at a current density of 1 mA cm⁻². The electrochemical impedance spectrum (EIS) spectrometry in Figure 3(c) shows 45-degree slanted curve, suggesting high Warburg resistance, and does not show any presence of semicircle in high frequency implying reduced capacitive behavior.^[36,37] This poor performance may be owed to the presence of mostly macropores and without sufficient micropores for effective ion diffusion.

The CV curve of LCF #3 shows a nearly rectangular shape with small deviation, suggesting the presence of pseudocapacitive behavior along with the EDLC behavior owing to the presence of oxygen containing functional groups and sulfur compounds.^[18,38] LCF #3 has a great charge-discharge efficiency, as signified by the near isosceles triangle shape of the GCD curve at different current densities in Figure 3(e). More importantly, the LCF #3 electrode delivers an excellent area capacitance of 19.78, 19.20, 18.43, 17.87 and 17.36 F cm⁻² at current densities of 1, 2, 5, 10, and 20 mA cm⁻², respectively. These values indicate a superior electrochemical behavior in the

LCF #3 electrode with a large thickness of 2.5 mm and high mass loading of 113 mg cm^{-2} . The obtained areal capacitance is higher than 6.20 F cm^{-2} at a current density of 1.4 mA cm^{-2} obtained from a free-standing lignin carbon electrode fabricated with Pluronic P123 polymer as a template and silica as a pore generator, as well as 5.88 F cm^{-2} at 1 mA cm^{-2} achieved in a thick lignin carbon electrode obtained in presence of Ni-foam.^[17] In addition, Figure 3(e) shows that the LCF #3 electrode has an excellent capacitance retention rate of 86.7% even at a high current density of 100 mA cm^{-2} . To our knowledge, these values are among the highest with comparable thickness and mass loading. The occurrence of a very small iR drop (7.3 mV) further confirms the high-rate performance of the electrode. The Nyquist plot in Figure 3(f) shows a typical capacitive curve. The small semicircle is followed by a short 45-degree phase shift segment implying small Warburg resistance. Furthermore, an almost vertical line parallel to the real X-axis indicates strong EDLC behavior. The equivalent series resistance (ESR) of the LCF #3 is as low as 1.15 ohm, enabling excellent ion transfer and conductivity.^[36,37] Even with the high mass loading of 113 mg cm^{-2} , the gravimetric capacitance is decent with 145.74 F g^{-1} at 0.5 A g^{-1} as presented in Figure 3(g). These high area and gravimetric capacitances account for the high-power density supercapacitors by tuning the amount of sodium in the electrode. The electrode has a great charging and discharging stability as 99.5% of initial capacitance is retained after 5,000 cycles (Figure 3i). The continuous increase in loading percentage of sodium into lignin carbon (e.g., ~28 wt.% for LCF #4) may further enhance the capacitance. However, a higher loading rate of sodium makes the carbon/sodium more brittle and susceptible to fracturing when the material is polished to a few millimeters in thickness. Therefore, the optimal sodium percentage is approximately 20%.

Electrochemical behavior refers to the chemical reactions that occur at the interface between an electrode and an electrolyte solution. The behavior of the system is influenced by the concentration of ions in electrolyte, as well as zeta potential of the electrode surface. To clearly understand the role of sodium in both LCF #1 and LCF #3 during electrochemical charging and discharging, the zeta potential was measured and shown in Figure 4. The zeta potential for LCF #1 is -13.88 mV (Figure 4b), whereas LCF #3 shows a more negative potential of -59.4 mV with a weaker peak at -87.4 mV (Figure 4d). The higher negative zeta potential in LCF #3 can be attributed to

the presence of sodium compounds^[25] and higher percentage of oxygen containing functional groups.^[39] As shown in EDS analysis, LCF #3 has more sodium content than LCF #1, leading to a larger gradient of sodium concentration. As a result, the concentration of OH^- increases in the Stern layer. This increase in ion concentration is easily accommodated in LCF #3 due to the presence of board pore distribution as shown in Figure 3(b). This board pore distribution facilitates better ion diffusion and conduction. Additionally, previous research suggests that the increase in negative zeta potential value will increase the conductivity of materials,^[39] which positively affects the capacitance of the material. Therefore, a great electrochemical capacitance is achieved in the electrode fabricated with LCF #3.

To quantify the role of hydroxyl group and sulfur compound in overall capacitance, the contribution of capacitive and diffusive capacitance on total capacitance for LCF #3 is summarized in Figure 5. The electrochemical kinetics of LCF #3 electrode is investigated based on the CV curves with scan rates from 1 to 20 mVs^{-1} . The contribution of the capacitive effect (pseudocapacitance) and diffusion-controlled capacity (EDLC) are quantitatively separated from the total charge storage based on Dunn's approach:

$$i(V) = k_1 v + k_2 v^{1/2} \quad (1)$$

The ratios of capacitive contribution can be calculated by separating the current response i at a fixed potential V into capacitive effects with a fast kinetics (proportional to the scan rate v) and diffusion-controlled reactions ($k_2 v^{1/2}$). By determining both k_1 and k_2 constants, the fraction of the current from surface capacitance and K^+ (potassium ion) semi-infinite linear diffusion can be distinguished. Figure 5(a-e) shows the typical voltage profile at different current densities for the diffusive current (light red region) in comparison with the total current. A dominant diffusive contribution (~73%) is obtained for the LCF #3 electrode at 1 mVs^{-1} as shown in Figure 5(a). As the scan rate increases, the role of capacitive contribution widens. The normalized contribution ratios of capacitive (light red) and diffusion-controlled (light blue) capacities at various scan rates are summarized in Figure 5(e). The capacitive capacity gains a maximum value of ~65% at 20 mVs^{-1} , which is reasonable since the diffusion-controlled EDLC originates from the electrostatic adsorption of charge-separated anions and cations. The

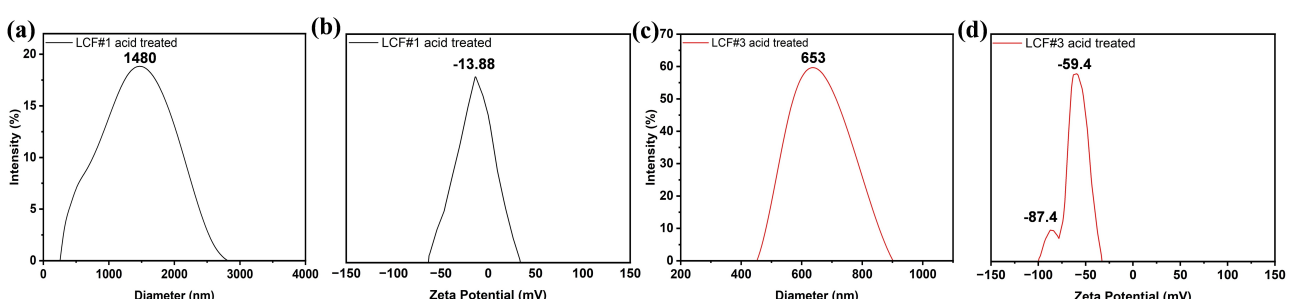


Figure 4. Zeta potential measurement. a) Particle size distribution and b) zeta potential of LCF #1 c) Particle size distribution and d) zeta potential of LCF #3

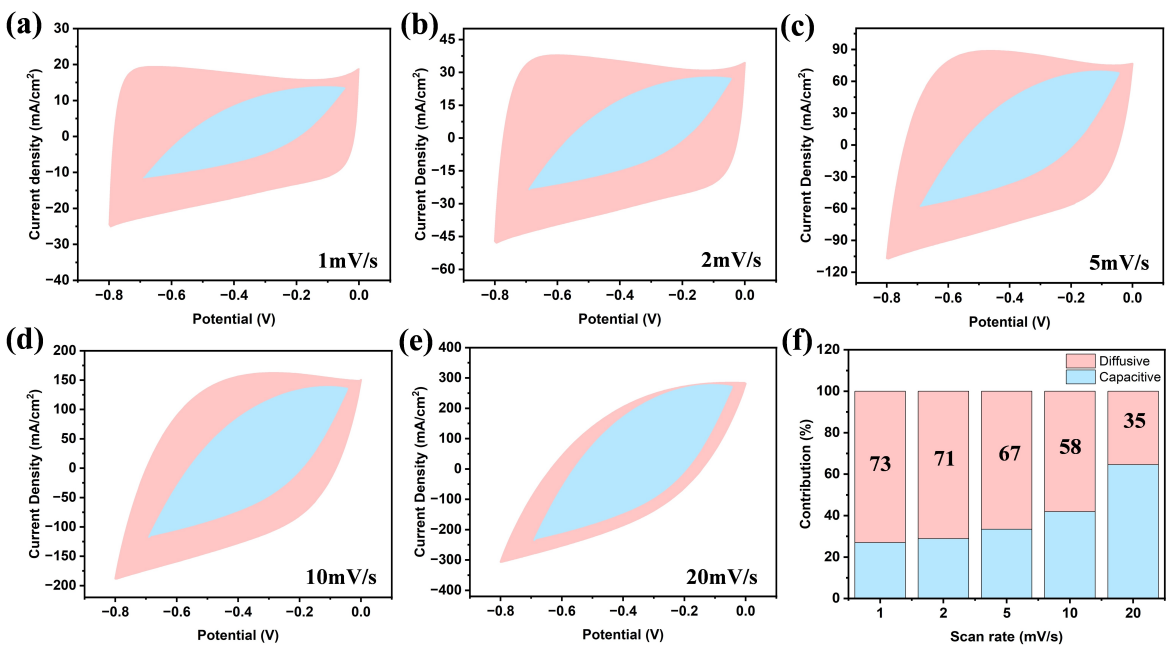


Figure 5. Kinetics of charge storage mechanism and quantitative analysis of capacitive (light blue) and diffusion (pink) capacities of LCF #3 at various scan rates: a) 1, b) 2, c) 5, d), and e) 20 mV s^{-1} . f) Normalized contribution ratio of capacitive and diffusion-controlled capacities at various scan rates.

charge separation is a slow electrochemical process compared with the pseudocapacitive faradaic reaction.

A supercapacitor device was assembled with two LCF #3 electrodes, a piece of cloth paper, and two pieces of Teflon plates, which illuminated an LED bulb. The demonstration can be found in the Supporting Information Section 7. To demonstrate the advantage by coupling lignin carbon and alkali metals, Figure 6 compares the electrochemical capacitance obtained from LCF #3 to previously reported data on different carbon materials with various thicknesses. The freestanding electrode combined lignin carbon with sodium yet without any binder and additives has the highest specific areal capacitance of 19.7 F cm^{-2} at a current density of 1 mA cm^{-2} . Taking account of thickness, the areal capacitance was normalized by dividing thickness to get volumetric capacitance, which is shown in

Figure 6(b). The fabricated electrode with LCF #3 still maintains superior capacitance.

Conclusions

In summary, we have established an important pathway to utilize biowaste lignin towards advanced energy storage. Free-standing 3D thick electrodes were designed and developed by combining lignin with various sodium contents. Sodium plays a key role in dictating surface morphology and chemical properties of the electrodes, which promotes the concentration of the OH^- ion in the Stern layer thus contributing to a promising capacitive performance. The as-synthesized freestanding 3D lignin/sodium electrode displays an exceptional specific areal capacitance of 19.7 F cm^{-2} at a current density of 1 mA cm^{-2} .

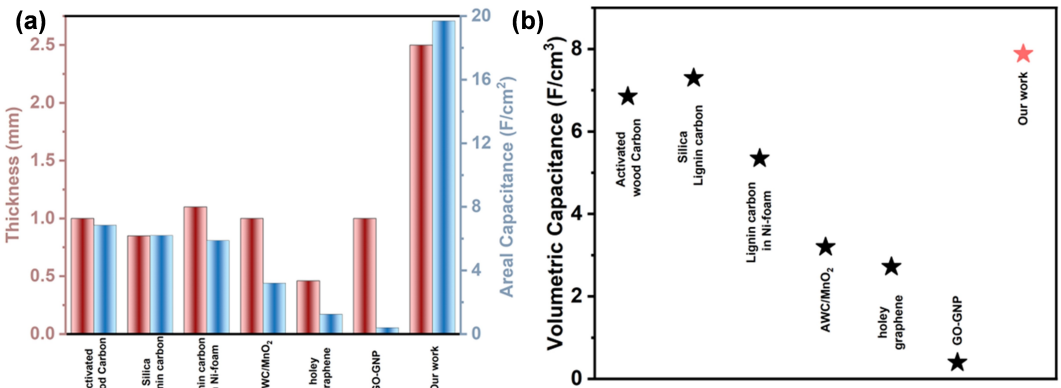


Figure 6. Comparison with other works. a) Areal capacitance vs. thickness. b) Volumetric capacitance.

along with a decent specific mass capacitance of 145.74 F g^{-1} at 0.5 A g^{-1} with mass loading of 113 mg cm^{-2} . The superior electrochemical performance of the lignin/sodium electrode is further demonstrated by an outstanding retention rate of 86.7% at 100 mA cm^{-2} and a great cyclic stability (99.5%). This work presents a new alternative to convert biowaste lignin into valuable products for fulfilling the ever-increasing demand on green energy storage devices.

Experimental Section

Raw materials: Kraft lignin (BioChoice lignin) was supplied by Domtar Inc. Sulfuric acid (99.99%) was obtained from Sigma-Aldrich, and hydrogen peroxide (37 wt.%) was acquired from Alfa Aesar whereas potassium hydroxide (KOH) pellets were purchased from EMD Millipore and made into solution in DI water.

Porous carbon preparation: The porous LCF samples were prepared similarly as described in our previous work.^[40] This study utilized two lignin precursors that differ from those used in previous work, with one containing 0.5 wt. % ash content and the other containing 4.5 wt. % ash content. The lignin precursors were first crashed to fine powder ($\sim 100\text{--}500 \mu\text{m}$). The lignin powder was then poured into a mold. The powder in the mold was cold pressed to a solid lignin block. The lignin block in the mold was placed into a furnace and heated to 450°C with 5°C min^{-1} heating rate and held for 1 hour. The pyrolysis lignin block was further carbonized at 1000°C for 1 hour before cooling down to room temperature. The porous carbon materials obtained from lignin with 0.5 wt. % ash content were designated as LCF #1, whereas those obtained from lignin with 4.5 wt. % ash content were denoted as LCF #3

Morphology, structure and composition characterizations: Morphology and composition of electrodes were characterized by scanning electron microscopy (SEM, Zeiss NVision 40 FIB/SEM) equipped with an energy dispersive X-ray (EDX) detector. Crystalline structure was characterized by XRD (Rigaku Ultima III, using $\text{Cu } K_\alpha$ radiation ($\lambda = 1.5406 \text{ \AA}$)). N_2 adsorption/desorption method (Micromeritics ASAP 2020) was utilized to characterize pore size and surface area of the samples. The specific surface area was calculated by the BET method, the pore size distribution and average pore size were calculated by density functional theory (DFT) method. The content and configuration of carbon, oxygen, and sodium were analyzed by XPS (PHI Quanter XPS with $\text{Al } K_\alpha$ X-ray). Water contact angle was measured by goniometer (DataPhysics Instruments, OCA 15EC). The level of defects for both LCF #1 and LCF #3 was evaluated by Raman spectrum (Horiba Ltd. XploRA plus Raman Microscope). The functional groups on LCF #1 and LCF #3 surface with and without acid treatment were investigated by Fourier transform infrared spectroscopy (FTIR, ABB FTIR 2000 spectrometer). Both LCF #1 and LCF #3 were grinded into particles and then mixed with KBr. The mixture was pressed into disc and spectra were recorded in the absorbance mode.

Electrode preparation for supercapacitors: The obtained lignin carbon foam was cut and polished to the size of $6.5 \text{ mm} \times 8.5 \text{ mm} \times 2.55 \text{ mm}$ (length \times width \times thickness) using 800–2000 grit sandpapers. The prepared electrode was submerged in piranha solution with 3:1 of concentrated sulfuric acid (99.99%) to 30 wt. % hydrogen peroxide overnight to increase hydrophilicity. The sample was washed multiple times in deionized (DI) water until the pH reached approximately 7, before putting into a PTFE holder as working electrode for electrochemical testing.

Electrochemical characterization: An electrochemical workstation (Chi 600E, Chi Instruments) with three-electrode configuration in

6 M KOH electrolyte was used to investigate the electrochemical properties. A platinum plate ($10 \text{ mm} \times 10 \text{ mm}$) and a saturated calomel were used as counter electrode and reference electrode respectively. Cyclic voltammetry (CV) was carried out in potential window from -0.8 V to 0 V to investigate the capacitive behavior. The scan rates varied from 1 mV s^{-1} to 20 mV s^{-1} . Similarly, galvanostatic charge-discharge (GCD) measurements were conducted with current densities increased from 1 mA cm^{-2} to 100 mA cm^{-2} to evaluate the areal capacitance of the electrodes. The electrochemical impedance spectrum (EIS) was examined at the open circuit potential with voltage amplitude of 5 mV , alternating current with frequency ranging from 0.01 Hz to 100 kHz . The areal and mass specific capacitances of the electrodes were calculated by following equations:

$$C_{(\text{areal})} = \frac{I}{(dV/dt) \cdot S} \quad (\text{a})$$

$$C_{(\text{mass})} = \frac{I}{(dV/dt) \cdot m} \quad (\text{b})$$

where I is the discharge current (A), dV/dt is the average slope of the discharge curve after deducting the ohmic drop (V/s), S is the effective area of the electrode (cm^2) and m is the mass of the electrode (g).

Zeta potential measurement: The zeta potential of the samples was measured in Malvern Zetasizer at a pH of 7. The mono suspension was obtained by dispersing the pulverized LCF #1 and LCF #3 in ethanol using ultrasonic homogenizer.

Supporting Information

Supporting Information is available from the Wiley Online Library or from the author.

Author Contributions

Z. C. and Y. Y. conceived and designed the project. Z. C. and Q. Y. designed and fabricated all LCF materials. M. N. supervised by Y. Y. carried out characterizations and conducted electrochemical testing. R. H., P. D. and Z. B. helped with BET characterizations. R. M. and M. N. supervised by C. T. performed zeta potential measurement. M. N. and Q. Y supervised by Y. Y., Z. C. and J. W. drafted the manuscript with input, discussion, and approval from all co-authors. M. N. and Q. Y. contributed equally to this work.

Acknowledgements

Z. C., J. W., Q. Y. and Y. Y. acknowledge the financial support from the USDA Forest Service through Grant Nos. 20-JV-11111124-035, 23-JV-11111124-005, and Wood Innovations Grant, No. 20-DG-11094200-234. The authors would like to acknowledge Domtar Corp., North Carolina for providing Kraft lignin for this study. Y. Y. and P. D. acknowledge the financial support from the Department of the Interior, Bureau of

Reclamation under contract R19AC00116. Special thanks are also given to Timothy Ketelboeter, and Joseph Destree at USDA Forest Products Laboratory, for their help in making this project run successfully.

Conflict of Interests

The authors declare no conflict of interest.

Data Availability Statement

Research data is available per request.

Keywords: lignin carbon • sodium • supercapacitors • areal capacitance

- [1] G. J. Ritter, *Ind. Eng. Chem.* **1925**, *17*, 1194–1197.
- [2] M. Lawoko, G. Henriksson, G. Gellerstedt, *Biomacromolecules* **2005**, *6*, 3467–3473.
- [3] F. G. Calvo-Flores, J. A. Dobado, *ChemSusChem* **2010**, *3*, 1227–1235.
- [4] P. Mousavioun, G. A. George, W. O. S. Doherty, *Polym. Degrad. Stab.* **2012**, *97*, 1114–1122.
- [5] C. Réti, M. Casetta, S. Duquesne, S. Bourbigot, R. Delobel, *Polym. Adv. Technol.* **2008**, *19*, 628–635.
- [6] J. Rajesh Banu, S. Kavitha, R. Yukesh Kannah, T. Poornima Devi, M. Gunasekaran, S.-H. Kim, G. Kumar, *Bioresour. Technol.* **2019**, *290*, 121790.
- [7] A. Lee, Y. Deng, *Eur. Polym. J.* **2015**, *63*, 67–73.
- [8] T. Kaneko, M. Matsusaki, T. T. Hang, M. Akashi, *Macromol. Rapid Commun.* **2004**, *25*, 673–677.
- [9] W. E. Tenhaeff, O. Rios, K. More, M. A. McGuire, *Adv. Funct. Mater.* **2014**, *24*, 86–94.
- [10] S. X. Wang, L. Yang, L. P. Stubbs, X. Li, C. He, *ACS Appl. Mater. Interfaces* **2013**, *5*, 12275–12282.
- [11] H. Lu, A. Cornell, F. Alvarado, M. Behm, S. Leijonmarck, J. Li, P. Tomani, G. Lindbergh, *Materials* **2016**, *9*, 127.
- [12] T. Chen, Q. Zhang, J. Pan, J. Xu, Y. Liu, M. Al-Shroofy, Y. T. Cheng, *ACS Appl. Mater. Interfaces* **2016**, *8*, 32341–32348.
- [13] F. Jianhui, Y. Boyuan, N. HaoXiong, H. Xiaojun, *IEEE* **2011**, *1*, 878–882.
- [14] W. Zhang, H. Lin, Z. Lin, J. Yin, H. Lu, D. Liu, M. Zhao, *ChemSusChem* **2015**, *8*, 2114–2122.
- [15] K. Wang, Y. Cao, Z. Gu, P. Ahrenkiel, J. Lee, Q. H. Fan, *RSC Adv.* **2016**, *6*, 26738–26744.
- [16] H. Li, Y. Zhao, S. Liu, P. Li, D. Yuan, C. He, *Microporous Mesoporous Mater.* **2020**, *297*, 109960.
- [17] S. Guo, H. Li, X. Zhang, H. Nawaz, S. Chen, X. Zhang, F. Xu, *Carbon* **2021**, *174*, 500–508.
- [18] Y. He, Y. Zhang, X. Li, Z. Lv, X. Wang, Z. Liu, X. Huang, *Electrochim. Acta* **2018**, *282*, 618–625.
- [19] L. F. Chen, X. D. Zhang, H. W. Liang, M. Kong, Q. F. Guan, P. Chen, Z. Y. Wu, S. H. Yu, *ACS Nano* **2012**, *6*, 7092–7102.
- [20] A. L. M. Reddy, S. Ramaprabhu, *J. Phys. Chem. C* **2007**, *111*, 7727–7734.
- [21] P. K. Nayak, L. Yang, W. Brehm, P. Adelhelm, *Angew. Chem. Int. Ed.* **2018**, *57*, 102–120.
- [22] Y. Wen, K. He, Y. Zhu, F. Han, Y. Xu, I. Matsuda, Y. Ishii, J. Cumings, C. Wang, *Nat. Commun.* **2014**, *5*, 4033.
- [23] A. B. Fuertes, M. Sevilla, *ACS Appl. Mater. Interfaces* **2015**, *7*, 4344–4353.
- [24] B. Mosallanejad, S. S. Malek, M. Ershadi, A. A. Daryakenari, Q. Cao, F. Boorboor Ajdari, S. Ramakrishna, *J. Electroanal. Chem.* **2021**, *895*, 115505.
- [25] S. Biswas, A. Chowdhury, A. Chandra, *Front. Mater.* **2019**, *6*, 54.
- [26] M. Kleen, G. Gellerstedt, *J. Anal. Appl. Pyrolysis* **1995**, *35*, 15–41.
- [27] J. Wang, M. Zhang, M. Chen, F. Min, S. Zhang, Z. Ren, Y. Yan, *Thermochim. Acta* **2006**, *444*, 110–114.
- [28] E. Raymundo-Piñero, P. Azaïs, T. Cacciaguerra, D. Cazorla-Amorós, A. Linares-Solano, F. Béguin, *Carbon* **2005**, *43*, 786–795.
- [29] M. Sevilla, A. B. Fuertes, *J. Mater. Chem. A* **2013**, *1*, 13738–13741.
- [30] W. Qian, J. Zhu, Y. Zhang, X. Wu, F. Yan, *Small* **2015**, *11*, 4959–4969.
- [31] A. Cao, C. Xu, J. Liang, D. Wu, B. Wei, *Chem. Phys. Lett.* **2001**, *344*, 13–17.
- [32] A. Harabor, P. Rotaru, A. Harabor, P. Rotaru, N. A. Harabor, *Physics AUC* **2013**, *23*, 79–88.
- [33] Q. He, R. He, A. Zia, G. Gao, Y. Liu, M. Neupane, M. Wang, Z. Benedict, K. K. Al-Quraishi, L. Li, P. Dong, Y. Yang, *Small* **2022**, *18*, 2200272.
- [34] J. Tian, Z. Liu, Z. Li, W. Wang, H. Zhang, *RSC Adv.* **2017**, *7*, 12089–12097.
- [35] W. Yan, X. Feng, X. Chen, W. Hou, J. J. Zhu, *Biosens. Bioelectron.* **2008**, *23*, 925–931.
- [36] B. N. M. Dolah, M. A. R. Othman, M. Deraman, N. H. Basri, R. Farma, I. A. Talib, M. M. Ishak, *J. Phys. Conf. Ser.* **2013**, *431*, 012015.
- [37] B. A. Mei, O. Monteshari, J. Lau, B. Dunn, L. Pilon, *J. Phys. Chem. C* **2018**, *122*, 194–206.
- [38] S. Shaheen Shah, S. M. Abu Nayem, N. Sultana, A. J. Saleh Ahammad, M. Abdul Aziz, *ChemSusChem* **2022**, *15*, e202101282.
- [39] C. Chen, L. Hu, *Adv. Mater.* **2021**, *33*, 2006207.
- [40] Q. Yan, R. Arango, J. Li, Z. Cai, *Mater. Des.* **2021**, *201*, 109460.

Manuscript received: May 10, 2023

Revised manuscript received: June 16, 2023

Accepted manuscript online: June 26, 2023

Version of record online: July 24, 2023